



Detailed flow physics of the supersonic jet interaction flow field

Valerio Viti, Reece Neel, and Joseph A. Schetz

Citation: [Physics of Fluids \(1994-present\)](#) **21**, 046101 (2009); doi: 10.1063/1.3112736

View online: <http://dx.doi.org/10.1063/1.3112736>

View Table of Contents: <http://scitation.aip.org/content/aip/journal/pof2/21/4?ver=pdfcov>

Published by the [AIP Publishing](#)

Copyright by the American Institute of Physics. Detailed flow physics of the supersonic jet interaction flow field. Viti, Valerio and Neel, Reece and Schetz, Joseph A., *Physics of Fluids (1994-present)*, 21, 046101 (2009), DOI:<http://dx.doi.org/10.1063/1.3112736>



Re-register for Table of Content Alerts

Create a profile.



Sign up today!



Detailed flow physics of the supersonic jet interaction flow field

Valerio Viti,¹ Reece Neel,² and Joseph A. Schetz³

¹*Department of Mechanical Engineering, University of Kentucky, Lexington, Kentucky 40506, USA*

²*AeroSoft, Inc., Blacksburg, Virginia 24060, USA*

³*Department of Aerospace and Ocean Engineering, Virginia Tech, Blacksburg, Virginia 24060, USA*

(Received 20 March 2008; accepted 26 February 2009; published online 16 April 2009)

The supersonic jet interaction flow field generated by a sonic circular jet with a pressure ratio of 532 exhausting into a turbulent MACH 4.0 cross flow over a flat plate was investigated using numerical simulations. The simulations made use of the three-dimensional Reynolds-averaged Navier–Stokes (RANS) equations coupled with Wilcox’s 1998 k - ω turbulence model. The numerical solution was validated with experimental data that include the pressure distribution on the flat plate, with an empirical formula for the height of the barrel shock, and with the Schlieren pictures showing the location and shape of the main shock formations. The simulations correctly captured the location and shape of the main flow features and compared favorably with the experimental pressure distribution on the flat plate. The validated numerical simulation was used to investigate in detail the flow physics. The flow field was found to be dominated by the shock formations and their coupling with the strong vortical structures. Three primary shock formations were observed: a barrel shock, a bow shock, and a separation-induced shock wave. While the general structure of the barrel shock was found to be similar to that of the underexpanded jet exhausting into a quiescent medium, two unique features distinguished the flow field: the concave indentation in the leeside of the recompression (barrel) shock and the folding of the windward side of the barrel shock due to an inner reflection line. The presence of the steep pressure gradients associated with the shocks creates strong vortical motions in the fluid. Six primary vortices were identified: (i) the well-known horseshoe vortex, (ii) an upper trailing vortex, (iii) two trailing vortices formed in the separation region and, aft of the bow shock wave, (iv) two more trailing vortices that eventually merge together into one single rotational motion. The low-pressure region aft of the injector was found to be generated by the combined effect of the concave indentation in the leeside of the barrel shock and the lower trailing vortices. The trailing vortices were found to be the main mechanism responsible for the mixing of the injectant with the freestream fluid. © 2009 American Institute of Physics.

[DOI: [10.1063/1.3112736](https://doi.org/10.1063/1.3112736)]

I. INTRODUCTION

The jet interaction flow field is the name given to the fluid dynamics phenomenon produced by a jet exhausting in a cross flow. This flow field can be found in several technological applications and, due to the presence of separated flows, vortical motions, turbulence, and, if the flow is supersonic shocks and expansion fans, is a formidable fluid dynamics problem. The AGARD conference proceedings¹ give an ample and detailed review of the range of possible applications. Examples range from the low-speed regimes of a chimney plume in a cross flow to the very high-speed regimes of scramjet combustion and missile control systems, from the low mass flow cases of boundary layer control systems and gas-turbine blade cooling to the high mass flow cases of a landing V/STOL vehicle. The basic problem of a fluid injected into a cross flow has several variables depending on its intended application: injector yaw and pitch angle, jet flow conditions (subsonic, sonic, and supersonic), freestream conditions (subsonic, supersonic, laminar, and turbulent), not to mention the phase and the chemical composition of the injectant (single or multiphase, nonreacting or reacting mixture, etc.).

The present study focuses on the case of sonic, normal

injection of a perfect gas through a circular injector into a MACH 4.0 turbulent cross flow over a flat plate. The ratio of the jet total pressure to the freestream static pressure, defined as the pressure ratio, is 532 as defined by Cubbison *et al.*² This configuration is representative of a typical reaction control system installed on a hypersonic vehicle. In reaction control systems, normal injection is usually chosen over angled injection because it maximizes the lateral force produced by the thrust of the jet. Two primary mechanisms contribute to the production of the lateral force.³ The first contribution comes purely from the thrust produced by the jet. The second contribution is produced by the complex interaction of the jet with the cross flow. The injected gas acts as an obstruction to the primary flow and, as such, produces a shock wave in the primary flow (see Fig. 1). The shock wave produces an adverse pressure gradient that causes the boundary layer on the wall to form a separation region ahead of the injector. The high pressures typical of recirculated flows (see Refs. 4–6) augment the lateral force produced by the thrust of the jet. Therefore, a jet operating in a cross flow over a flat surface at zero angle of attack will produce a larger force than if it was exhausting into a quiescent medium.³ However, concurrent with the separation region, a large wake with a

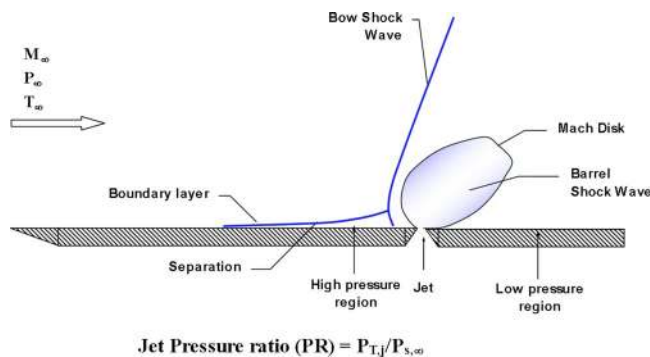


FIG. 1. (Color online) Schematic of the flow field along the tunnel center line. The definition of the jet PR proposed by Cubbison *et al.* (Ref. 2), is used throughout this paper.

low-pressure region forms aft of the injector, as described by Spaid *et al.*⁴ The low-pressure region has two main effects on the forces and moments produced by the jet on the surrounding surface. The first effect is to decrease the normal force on the plate.⁷ The low-pressure region effectively creates a suction behind the jet and, even though the suction is not strong it acts over a large area aft of the injector thus creating a strong upward force. The second, and in many aspects most detrimental effect is the coupling with the high-pressure region ahead of the jet and the formation of a nose-down moment about the injector. The contribution to the nose-down moment from the low-pressure region is particularly high since this region extends far aft of the injector.^{5,8} This shift in the center of pressure of the vehicle has to be corrected through the use of an attitude control system that actuates counterbalancing jet thrusters. The region of low-pressure aft of the injector corresponds, in part, to the wake behind the injector. The flow field in the wake is dominated by the presence of strong vortical motions that are formed in the boundary layer separation and by the barrel shock and that are convected downstream by the free stream. The detachment of the barrel shock from the surface of the flat plate forces these trailing vortices closer together and toward the solid surface, thus enhancing the longitudinal rotation of the fluid aft of the injection.

While in the low-speed jet interaction case the flow field can be largely modified by changing the injector geometry,⁹ in the high-speed jet interaction regimes the hole geometry does not have a strong influence on the flow field.¹⁰ The undesirable effects created by the jet interaction flow field can be mitigated by designing the surface around the injector in such a way as to modify the local flow field. A properly designed surface requires detailed knowledge of the flow field and of the flow structures responsible for the generation of the low- and high-pressure regions. Once these structures are well understood, they can be altered or removed to improve the functionality and performance of the whole injection system. A number of investigations aimed at the development of thrust vector control systems were carried out in the 1960s to study the pressure distribution in the region around the injector and the resulting normal force and pitching moment.^{4,11,12} Several researchers^{10,11,13–18} analyzed this flow field through analytical models and experiments. How-

ever, these efforts have been only partially successful due in large part to the difficulty of experimentally measuring the local flow without disrupting it and in part, due to the inherent complexity of the flow physics involved. Byun *et al.*¹⁹ attempted to decrease the area of low pressure by inserting a solid ramp aft of the injector. Conversely, Viti *et al.*⁸ suggested that the same effect as a solid ramp could be obtained by using a concept similar to the “aeroramp,”^{20,21} which consists in inserting smaller secondary injectors in the region aft of the main injector.

The present work aims at producing a detailed physical analysis of the supersonic jet interaction flow field through the use of computational tools. Such an analysis can improve the understanding of the relevant flow structures responsible for the generation of the pressure field and for the mixing of the injectant with the cross flow, ultimately improving present-day jet-thruster configurations and contributing to the understanding of scramjet fuel injection systems.

II. GOVERNING EQUATIONS, COMPUTATIONAL GRID, AND BOUNDARY CONDITIONS

The governing equations of a compressible turbulent flow can be written using time-averaged (Reynolds-averaged, indicated by an overbar) values of the density, pressure, and mass-weighted (Favre-averaged, indicated by a tilde) averages for the velocity components and temperature. Following, the governing equations used in this study are presented in their differential form.

Conservation of mass,

$$\frac{\partial \bar{\rho}}{\partial t} + \frac{\partial (\bar{\rho} u_i)}{\partial x_i} = 0. \quad (1)$$

Conservation of momentum,

$$\frac{\partial \bar{\rho} \tilde{u}_i}{\partial t} + \frac{\partial (\bar{\rho} \tilde{u}_i \tilde{u}_i + \bar{p} \delta_{ij})}{\partial x_i} = \frac{\partial}{\partial x_i} (\tilde{\tau}_{ij} + \tilde{\tau}_{ij}'') - \frac{\partial (\bar{\rho} \tilde{u}_i u_j'')}{\partial x_i}. \quad (2)$$

Conservation of energy,

$$\frac{\partial \bar{\rho} \tilde{e}_o}{\partial t} + \frac{\partial (\bar{\rho} \tilde{e}_o \tilde{u}_i + \bar{p} u_i + \bar{\rho} \tilde{e}_o u_i'')}{\partial x_i} = \frac{\partial}{\partial x_i} (\tau_{ij} u_j) - \frac{\partial \bar{q}_i''}{\partial x_i}, \quad (3)$$

where

$$\tilde{e}_o = \bar{C}_v \tilde{T} + \frac{1}{2} \tilde{u}_i \tilde{u}_i + \frac{1}{2} \tilde{u}_i u_i''. \quad (4)$$

The perfect gas law is used to close the system,

$$\bar{p} = \bar{\rho} R \tilde{T}. \quad (5)$$

The Reynolds-stress tensor is defined as

$$\tau_{ij} = -\bar{\rho} \tilde{u}_i u_j''. \quad (6)$$

In the above expressions, the tensor u_i represents the x , y , and z components of the velocity in a Cartesian coordinate system, T is the static temperature, C_v is the specific heat at constant volume, R is the gas constant (286.7 kJ/kg K), ρ is the fluid density, μ is the fluid laminar viscosity, and q is the heat flux.

The numerical calculations performed in this study used Wilcox's $k-\omega$ (1998) turbulence model.^{22,23} This model was

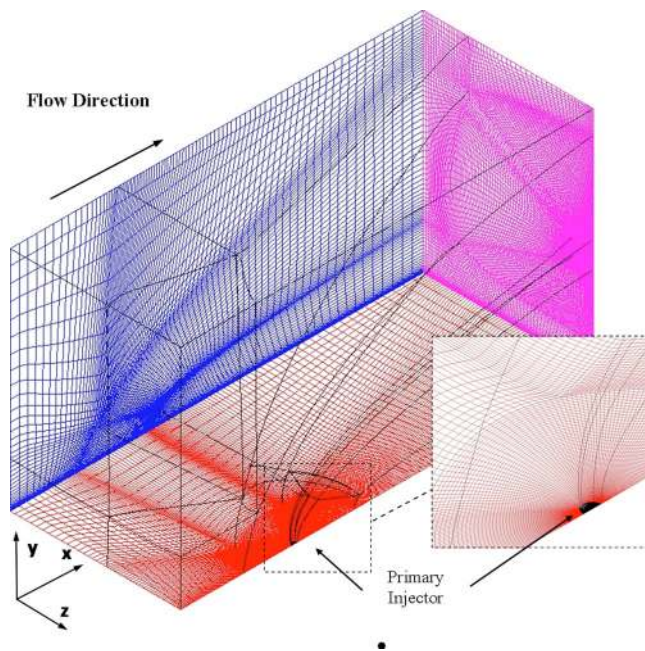


FIG. 2. (Color online) Isometric view of the structured computational grid composed of a combination of *C*-type and *H*-type grid topologies for a total of 13 zones. The inset shows detail of the *C*-type grid wrapping around the primary injector. Total number of cells is 1.54×10^6 cells, the surface mesh shows every other computational cell.

chosen because of its good ability in predicting separation and in dealing with adverse pressure gradients and separated flows compared to other two-equation models^{23–25} and to Wilcox’s Reynolds-stress transport model.²⁶ In particular, when compared to the more advanced eddy-viscosity model of Menter (Menter’s shear stress transport model²⁷), it appears that at least for the case of compressible jet interaction flow fields, the Wilcox model has better predicting capabilities.²⁴

The numerical solver used in this study is AeroSoft’s GASP version 4.0. GASP was chosen because it is a mature program with a proven reliability record in simulations of turbulent flows,²⁸ vortical flows,²⁹ jets,³⁰ shock-vortex interaction,³¹ and jet interaction flows.^{7,8,32} GASP solves the discretized integral form of the time-dependent Reynolds-averaged Navier–Stokes (RANS) equations over a structured grid.^{33,34}

The solution was driven to a steady-state using the implicit Gauss–Seidel scheme³⁵ and a Courant–Friedrich–Levy (CFL) number of 0.75. The relatively low CFL number was used in order to converge the solution without convergence problems which were observed during the initial iterations. The convective fluxes were computed using the flux-vector splitting of Roe with third order spatial upwind-biased accuracy using the Min-Mod limiter. The viscous terms were discretized using a second-order-accurate central differencing scheme. An exception to this flux combination was the replacement in the radial direction of the *C*-type zone that surrounds the injector of the Roe flux with the Van Leer flux leaving all the other parameters unchanged in order to avoid the “carbuncle effect.”³⁶ The computational grid used in this work is a combination of *H*-type and *C*-type grids shown in

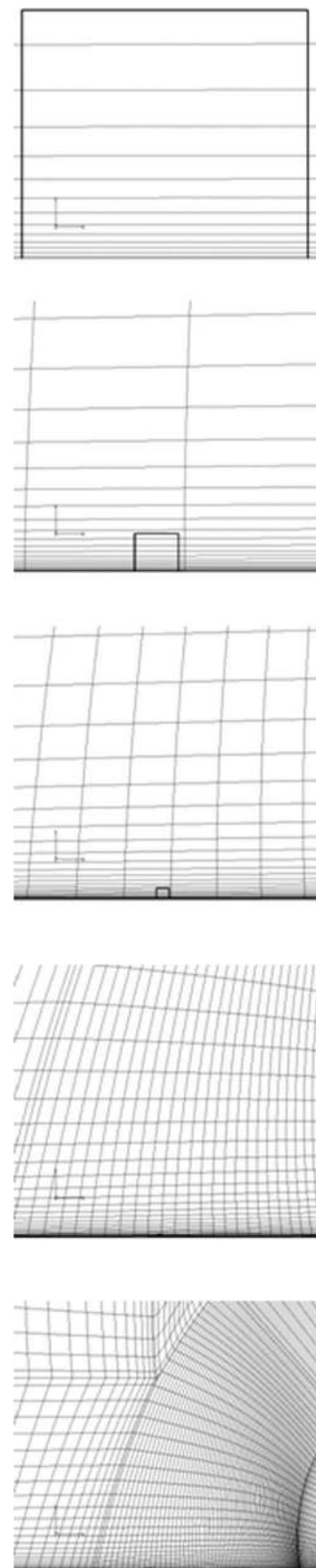


FIG. 3. Blow-up sequence showing the mesh close to the solid surface of the flat plate.

Fig. 2 that allows an optimal cell clustering around the injector. The grid size was dictated by the need to find a balance between the refinement of the grid and the CPU resources available for these runs. The grid was created using

TABLE I. Computational domain dimensions.

Parameter	Dimensions
Streamwise length, Δx	27.69 cm ($58x/d_j$)
Height, Δy	15.24 cm ($32y/d_j$)
Width, Δz	11.43 cm ($24z/d_j$)

GRIDGEN version 13.3.³⁷ Care was taken to ensure that the cells closest to the solid surface would lie below a y^+ of 1.0. One-dimensional hyperbolic tangent stretching³⁸ was used in all regions with a different stretching parameter to smoothly distribute the cells without steep changes in cell size. An example of this distribution close to the injector is given in Fig. 3. The first cell height was 1.8×10^{-6} m and the ratio of the second to first cell height was in the order of 2.0. The injector was simulated by cells on the surface of the flat plate with an imposed pressure and velocity equal to the jet total conditions. To help with convergence rate, the grid was sequenced twice by eliminating every other cell in the three spatial directions. The sequencing procedure generated a numerical solution on three grids with the same topology but different number of cells.

The computational domain for the flat plate with normal injection consisted of a six-sided box, 27.69 cm long, 15.24 cm wide, and 11.43 cm high, as shown in Fig. 2 and as described in Table I. The plate dimensions are listed in Table II and a full set of jet and freestream conditions can be found in Table III. The lower plane, i.e., the plane defined by $y/d = 0.0$, corresponds to the solid surface of the flat plate. Adiabatic wall ($\partial T / \partial y = 0.0$), no-slip conditions ($u = v = w = 0.0$) were imposed on the flat plate. The adiabatic wall condition is an approximation for the low-heat flux measured during experimental runs in the wind tunnel. The circular injector is cut flush in the surface of the flat plate and sonic conditions were applied at the cells simulating the jet ($Ma_J = 1.00$, $\rho_J = \rho^*$, $u_J = w_J = 0.0$ m/s, $v_J = v^*$, and $p_J = p^*$). The jet pressure ratio, $PR = P_{j,t} / P_\infty$, was 532 and the momentum flux, $\bar{q} = (p \gamma M^2)_j / (p \gamma M^2)_\infty$, was 17.4. The jet was assumed to have a step profile, i.e., no boundary layer profile in the nozzle was simulated. The area of the simulated jet is smaller than the jet used in the experiments and the ratio of the two areas is equal to the nozzle discharge coefficient (Cd_J), which was estimated through the use of numerical simulations to be 0.78.⁶ As a consequence, the injector in the tunnel had a diameter of 4.76 mm and the one in the present computations 4.12 mm, the two diameters related by $d_{j,CFD} = Cd_J^{0.5} d_{j,expt}$. By doing this, the viscous effects inside the nozzle were taken into consideration, and the mass flow of the simulated

TABLE II. Flat plate and injector dimensions.

Parameter	Dimensions
Flat plate entry length, x_0	7.62 cm
Injector diameter, d_j	0.476 cm
Injector effective diameter, $d_{j,e}$	0.412 cm
x_0/d_j	16.0

TABLE III. Summary of freestream and jet conditions.

Parameter	Conditions
(a) Free stream	
Gas	Air, perfect gas ($\gamma = 1.40$, $Pr = 0.72$, $R = 286.7$ J kg K)
M_∞	4.0
$P_{\infty,t}$	1120 kPa
P_∞	7.1 kPa
T_∞	70.3 K
Inlet δ	1.65 cm
(b) Jet conditions	
Gas	Air, perfect gas ($\gamma = 1.40$, $Pr = 0.72$)
M_j	1.0
$P_{j,t}$	3797 kPa
P_j	2006 kPa
T_j	261 K
$P_{j,t} / P_\infty$ (PR)	532
Momentum ratio	17.4
Jet mass flow	0.116 kg/s
Jet thrust	37.5 N

jet was the same as the real jet. Previous work on the effect of a velocity profile for the choked nozzle showed little or no effect on the shock formations in the cross flow.⁶ The flow upstream of the injector is supersonic, and a turbulent boundary layer is present. All the dependent variables at the inlet outside the boundary layer were assigned their respective freestream value corresponding to a MACH 4.0. The initial freestream turbulence intensity (TI) was assumed to be 5% since no turbulence measurements were available. This value was thought to be a reasonable assumption given the tunnel conditions. From this value and the assumption that the initial turbulent viscosity, μ_t , is 1/10th the laminar viscosity, it was possible to calculate the initial turbulent kinetic energy [$k = \frac{3}{2}(TI \cdot U_\infty)^2$] and turbulent frequency ($\omega = C_\mu \rho k / \mu_t$). Considering Wilcox's $k-\omega$ sensitivity to the freestream conditions, the forces and moments on the flat plate might have been affected by fixing the inlet turbulence level.³⁹ However, only the *initial* inlet turbulence level was specified. That is

TABLE IV. Grid convergence study results, normal force coefficient, C_{Fy} (top), and pitching moment coefficient, C_{Mz} (bottom).

Grid sequence	No. of cells	C_{Fy}	Difference (%)	Normalized C_{Fy}
Coarse	24 127	1.01	-6.6	0.94
Medium	193 012	1.06	-1.6	0.99
Fine	1 544 098	1.07	-0.6	1.00
	$f_{\text{exact, Richardson}} =$	1.08	0	1.01
Grid sequence	No. of cells	C_{Mz}	Difference	Normalized C_{Mz}
Coarse	24 127	11.76	-7.0	0.93
Medium	193 012	12.51	-1.1	0.99
Fine	1 544 098	12.64	-0.1	1.00
	$f_{\text{exact, Richardson}} =$	12.64	0	1.00

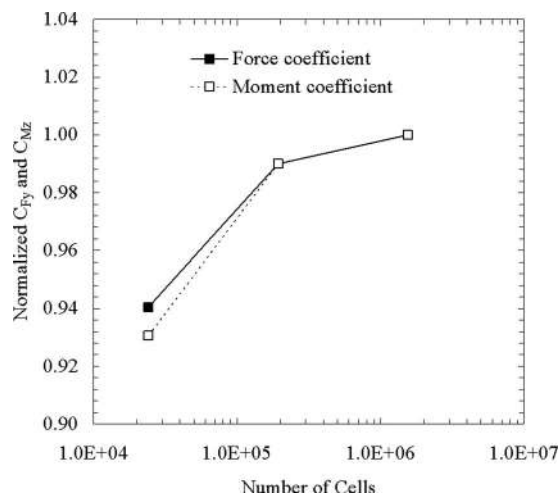


FIG. 4. Results of the grid-convergence study. The moment and force coefficients are normalized using the results from the fine grid (1.56×10^6 cells).

the inlet TI was fixed only during the very first iteration, and then the inlet turbulence level was extrapolated from the interior turbulence quantities. In this way the inlet TI was not preset and could adjust and relax to the proper level. In light of this approach, the final solution is not affected by the initial freestream TI. Due to restrictions in computational resources, a sensitivity analysis of forces and moments to the *initial* freestream TI was not performed. No TI was measured during the experiment and therefore it was not possible to make a more precise assumption or a direct comparison of the test and CFD turbulence levels. The entry boundary layer thickness, δ , was obtained from the Schlieren pictures of the tunnel flow, and the boundary layer velocity profile was assumed to follow the $1/7$ th power-law relationship. The assumption of the turbulent boundary layer profile combined with the length of the computational domain ahead of the separation region allows the boundary layer to develop to its proper equilibrium state before it separates.

The symmetry plane is represented by the x - y plane. The three remaining sides of the computational domain (the downstream exit plane, the top surface, and the longitudinal plane opposite the symmetry plane) do not represent any physical surface. The top surface and the sidewall of the wind tunnels were assumed to be distant enough from the injector not to interfere with the flow field of interest. Following this assumption the computational domain was smaller than the wind tunnel cross section and a first-order extrapolation boundary condition was applied to the top and side boundaries of the computational box as well as to the downstream exit plane.

The iterative convergence of the calculations was determined by checking the variation over time of the residuals of the five RANS equations and of the turbulent equations plus several flow parameters. Convergence was declared when the residuals, normal force, axial force, pitching moment, pressure distribution, and skin friction coefficient along the center line ahead of the injector were steady or showing a small-amplitude periodic behavior about a fixed value.⁵ The discretization error of the computations was calculated using

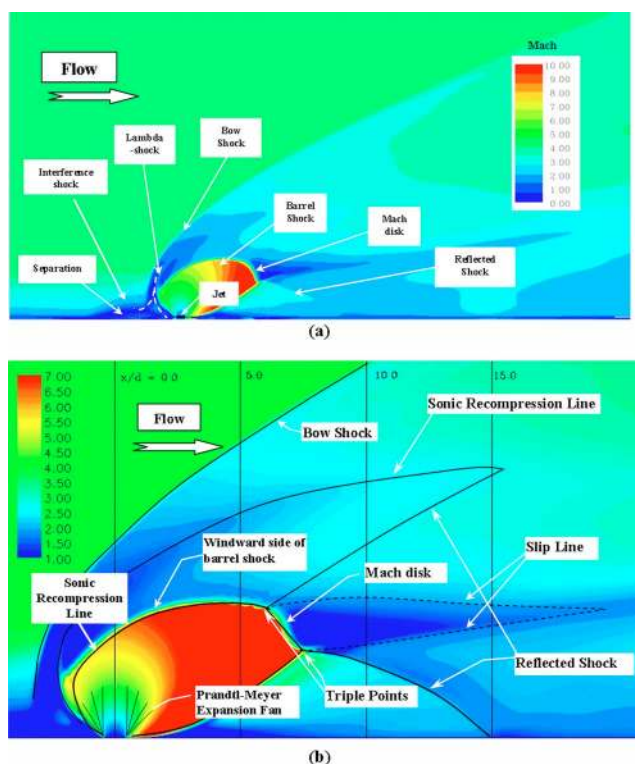


FIG. 5. (Color online) Mach contours on the plane of symmetry of the jet. Part (a) shows large-scale view and part (b) shows the detail of the flow field around the injector with the main flow features highlighted with solid lines. The solid lines are sketches indicating the recognizable flow patterns typical of the underexpanded jet exhausting in a quiescent medium.

the “mixed first+second order Richardson extrapolation” described by Roache⁴⁰ and Roy.⁴¹ The procedure made use of the solution and of the ratio of the number of cells on the three grid sequences to estimate the discretization error. The results of the grid-convergence study performed on the computational mesh of this work are tabulated in Table IV, including the “exact” solution computed via the Richardson extrapolation, and the same data are plotted in Fig. 4. The plot shows the change in normal force coefficient and pitching moment coefficient as the grid is refined from a coarse grid level with 2.4×10^4 cells to the medium grid level, 1.93×10^5 cells to the fine grid level, 1.54×10^6 . The change in the results from one grid level to the next is an indication of the error given by the discretization of the computational domain. The discretization error on the fine grid was estimated to be 0.6% for the normal force and 0.1% for the pitching moment (see Table IV). It should be noted that the mesh topology shown in Fig. 2 was the final result of an iterative mesh-optimization process in which the mesh density was increased or decreased according to the flow gradients obtained on a previous mesh topology. This process was repeated several times during the initial stages of the present work, starting from an initial multiblock Cartesian mesh and ending with the efficient mesh topology and cell distribution shown in Fig. 2. Complete details of the mesh-optimization process and of the estimation of the uncertainty can be found in Ref. 6.

Depending on the inlet conditions during tests, the flow

field is not steady and shows periodic asymmetries about the jet centerline.^{42–44} However, the RANS simulations did not capture the flow unsteadiness also when running the full three-dimensional (3D) domain and perturbing the inlet conditions. Therefore, it seemed appropriate to assume a steady-state flow field and make use of a symmetry boundary condition along the domain center line. While these two assumptions would not be adequate for extracting detailed time-accurate information, they are an adequate assumption for capturing and analyzing the main flow features.

III. RESULTS

This section presents the results and discussion based on the numerical simulation of the jet interaction flow field produced by normal sonic injection into a MACH 4.0 cross flow with a jet pressure ratio (PR) of 532 (see Table III). A general description of the jet interaction flow field based on the work of other researchers was given in Sec. I and some of its basic characteristics were schematically shown in Fig. 1. In Secs. III A–III E the flow field is analyzed more in depth with focus on the compressible features and the vortical structures which are the main mechanisms responsible for the formation of the pressure field on the solid surface surrounding the injector and for the mixing of the jet fluid with the cross flow.

A. Main flow features of the supersonic jet interaction flow field

A general view of the main features that characterize the supersonic jet interaction flow field is provided by the mapping of the Mach number contours on the plane of symmetry of the computational domain, Fig. 5(a). The sonic jet exhausting at a right angle into the supersonic cross flow produces an inclined barrel shock that, due to the jet being highly underexpanded, terminates in a Mach disk. A reflected shock is formed downstream of the barrel shock wave and it impinges on the flat plate. The barrel shock acts as a blunt body obstruction to the incoming flow thus forming a detached bow shock. A fully developed turbulent boundary layer is present at the upstream inlet and, as it approaches the adverse pressure gradient created by the bow shock wave, it separates from the tunnel flow, see contours of TI in Fig. 6. Figure 5(b) is a detailed view of the Mach contours around the injection location. The superimposed black lines help identifying the main structures that are typically found in an underexpanded sonic jet exhausting in a quiescent medium (see Ref. 45). However, different from the case of the sonic jet exhausting in a quiescent medium the backpressure is not uniform around the expanding jet due to the presence of the cross flow, the backpressure being higher on the windward side than on the leeward side of the plume. This nonuniformity of the backpressure causes the jet plume to trail downstream and to lose its axial symmetry. Looking at the interior volume of the barrel shock, a large expansion fan is present with its boundaries defined by a recompression shock that ends with a Mach disk. The Mach disk is essentially a normal shock that slows down the highly supersonic flow inside the plume to subsonic. The subsonic flow that is generated

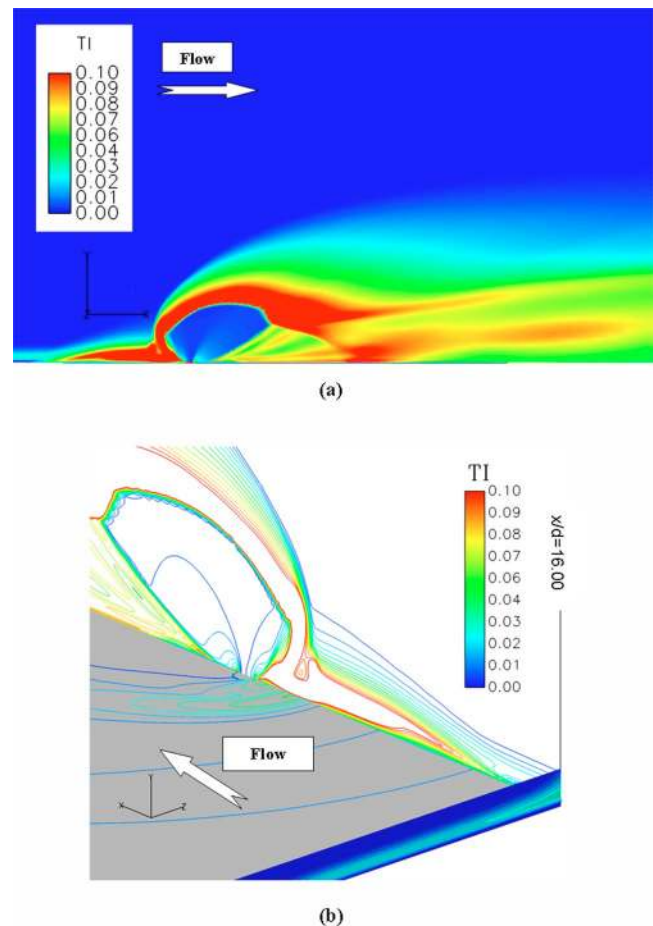


FIG. 6. (Color online) TI contours (a) on the plane of symmetry and (b) as seen in an isoview of the detailed area at the inlet. The colors on the surface of the flat plate represent pressure coefficient and are used for illustration only in this caption.

by the Mach disk forms a slip surface with the supersonic fluid flowing around and past the barrel shock. The slip surface is clearly visible in the Mach contours of Fig. 5(b). The two streams eventually mix together into a highly turbulent flow further downstream. According to Woodmansee *et al.*,^{45,46} a sonic line should envelope the barrel shock on its sides. Because of the mixing with the cross flow and the presence of the bow shock, it is difficult to identify the sonic line and the outer shear layer of the jet plume as described by Woodmansee *et al.* The windward side of the barrel shock appears to have less resemblance to the underexpanded jet flow field than the leeward side mainly because of the strong influence of the bow shock. A smeared sonic recompression line can be seen on the windward side of the barrel shock, generating from the windward side of the injector and extending past and above the barrel shock. A sonic recompression line does not form on the leeward side of the barrel shock due to the presence of the solid wall. The location where the downwind side of the barrel shock intersects the Mach disk is known as the triple point. A reflected shock extends downstream from this point and it impinges on the surface of the flat plate at $x/d=15.0$. This location can be clearly identified by the sudden pressure increase in the C_p plot of Fig. 7(b). The adverse pressure gradient produced by

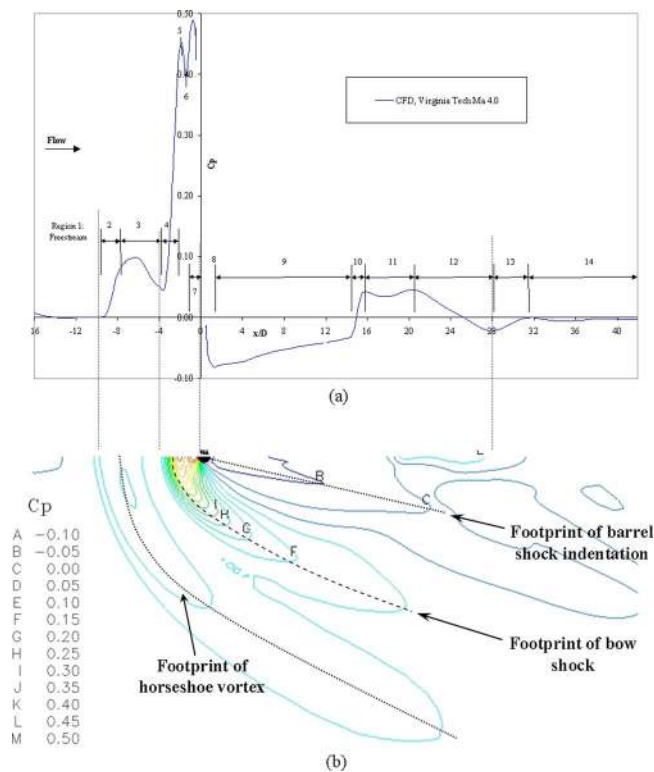


FIG. 7. (Color online) (a) Pressure coefficient distribution along the tunnel centerline and (b) pressure coefficient mapping on the surface of the flat plate.

the impingement of the reflected shock on the flat plate causes the boundary layer to thicken suddenly, as indicated by the plot of the Mach contours. On the upstream side of the barrel shock, the triple point can be easily located but the reflected shock extending from this location is barely identifiable. As mentioned before, this is a result of the strong interference created by the cross flow and the bow shock.

The strength of the bow shock varies depending on its location relative to the barrel shock. The bow shock is strongest along the plane of symmetry upstream of the barrel

shock, where it is basically a normal shock. Away from this location, the bow shock curves downstream in both the lateral and vertical directions, thus forming a wrapping surface around the barrel shock. Immediately aft of the normal shock section, local regions of subsonic flow are formed, and this flow is accelerated back to supersonic speeds by mixing with the supersonic cross flow fluid that has passed through the oblique sections of the bow shock.

Figure 5(a) places in evidence the lambda shock as it is often referred in literature. The Mach number contours along the plane of symmetry show that the two shocks never merge. This observation is contrary to what can be observed in shadowgraphs and Schlieren pictures where the two shocks appear to merge. The merging of the shocks observed in the experiments is likely due to the optical “collapse” of a 3D flow field on the two-dimensional plane of the photographs. This region has been studied by several works due to the complexity of the microflow structures that form between the two shocks (see Ref. 47).

Figure 6(a) shows the contours of the TI [$TI = (\frac{2}{3}k)^{0.5}/U_\infty$] on the plane of symmetry. As expected, the TI is particularly high in the areas with high velocity gradients, such as in the separation region, across and downstream of the shocks, and in the wake of the barrel shock where strong vortical structures are present and most of the mixing is occurring. At the inlet plane a turbulent boundary layer has developed from the initial guess of (i) a power-law velocity profile and (ii) a uniform 5% TI profile, as showed in the mappings of Fig. 6(b). The turbulent boundary layer is undisturbed in the region away from the center line while close to the center line, its thickness rapidly increases due to the presence of the adverse pressure gradient created by the presence of the jet. The TI distribution observed in the boundary layer mapping is typical of that for the flat plate with the locus of maximum turbulence level located at a distance above the solid surface.²³ This is clearly seen in Fig. 8(a) where the TI profiles at the inlet plane are plotted for different spanwise locations with $z/d=0.0$ representing the center line. The vertical axis is normalized using the measured

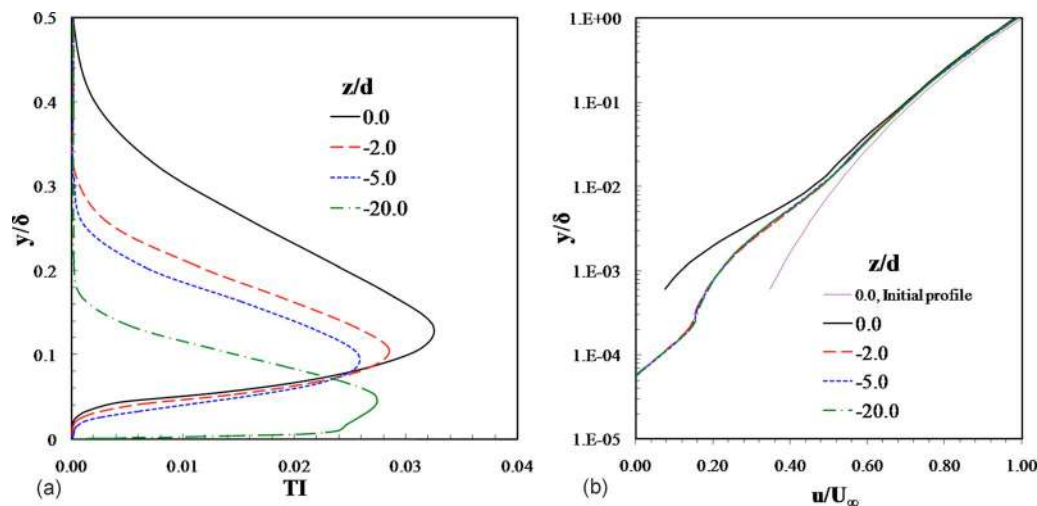


FIG. 8. (Color online) Converged inlet boundary layer profiles at different cross flow locations for (a) TI and (b) velocity. $z/d=0.0$ corresponds to the center line.

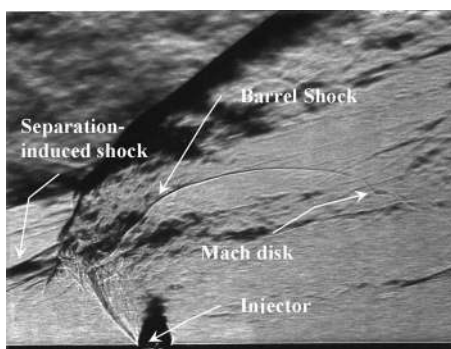


FIG. 9. Experimental Schlieren photograph of the jet interaction flow field, $Ma=4.0$, $PR=532$ [see Viti *et al.* (Ref. 8) and Wallis (Ref. 48)].

boundary layer thickness of 1.65 cm (see Table III). From these profiles it is clear that the initial estimate of a uniform TI of 5% has adjusted accordingly to the flow solution inside the domain and the maximum TI is now 3.2% along the center line. As noticed in the mappings of Fig. 6(b) the region of maximum turbulence in the boundary layer gets closer to the solid surface with the distance from the center line due to the decrease in the effect of the adverse pressure gradient created by the bow shock. Also, the freestream TI from the initial estimate of 5% has dissipated to a uniform value of 0.014%. The velocity profiles for the same locations, shown in Fig. 8(b), corroborate the finding that the propagation of the effects of the jet-induced separation to the inlet plane is limited to the region next to the center line and shows that the velocity profiles away from the center line remain practically undisturbed.

B. Validation of the numerical solution

The experimental data available for the case under investigation (see Ref. 48) are limited and, more importantly for this work, it was affected by large uncertainties due to the pressure-sensitive paint (PSP) used in the measurements. As a consequence of the limited data available, it was not possible to conduct an exhaustive quantitative validation of the numerical simulation and a limited qualitative validation study is conducted by comparing the CFD solution to the experimental Schlieren photographs of the flow field.^{5,6} The Schlieren photograph is shown in Fig. 9. The picture provides a means to draw an outline of the main flow features visible in the experiment such as the barrel shock, the bow shock and the separation-induced shock. Schlieren photographs depict the first spatial derivative of the density. Therefore, this derivative can be computed from the CFD simulations and the flow field features visible in the photograph of Fig. 9 can be superimposed on the numerical mapping. It is important to remember that while the Schlieren picture is a two-dimensional representation of a 3D flow, the CFD solution shown is an actual real two-dimensional slice through the 3D flow field. For this reason, some of the flow features visible in the Schlieren photographs that may appear to lie on the symmetry plane in actuality do not lie on it and cannot be directly compared to the CFD mappings on the symmetry

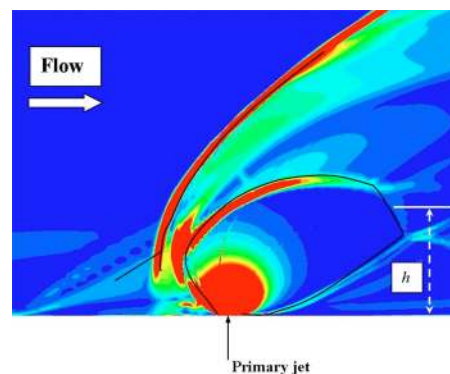


FIG. 10. (Color online) Comparison of the Schlieren picture with the CFD solution on the plane of symmetry. The CFD contours represent the magnitude of the first-derivative of the density with respect to space, $|\nabla\rho|$.

plane. Further, the Schlieren picture is an instantaneous snapshot of the flow field while the CFD picture represents a time-averaged solution. The comparison of the Schlieren photograph to the numerical solution is shown in Fig. 10. The CFD simulation correctly predicted the location of the separation-induced shock (near the location where it impinges on the bow shock), the location and shape of the bow shock, and of the barrel shock. Also, the Mach disk height over the flat plate, h , see Fig. 10, is in agreement with the measurements of Schetz *et al.*,¹² which uses the concept of equivalent backpressure, $P_{eb}=0.8P_{t,2}$, where $P_{t,2}$ is the total pressure behind a normal shock, for correlating the penetration height of a highly underexpanded jet to the Mach disk height. In the present case, the ratio P_j/P_{eb} was calculated to be 16.5, which correlates to a Mach disk height of $4.3h/d_j$, while the CFD predicted a Mach disk height of approximately $4.5h/d_j$. A comparison of the pressure field predicted by CFD with the experimental results is presented in Figs. 11(a) and 11(b). Figure 11(a) shows the mapping of the pressure coefficient extracted from the PSP data at the top half of the picture to the computed one, at the bottom half of the picture. The comparison highlights the qualitative agreement between the experiment and the CFD. However the PSP data present (i) a high level of experimental noise as evidenced by the fragmented isolines and (ii) a lack of resolution, shown by the lack of the high-pressure region in the separation ahead of the injector. The latter point can help explain the large discrepancy between the PSP and the CFD solution in the region immediately in front of the jet, $-3.0 < x/D < 0.5$. Other CFD studies of the supersonic jet interaction flow field with more accurate surface pressure experimental data (see Refs. 24 and 49) have observed a pressure distribution which resembles very closely that predicted by the present numerical simulations. It must be noted that both the Tam and Chenault cases had much lower jet pressure ratios than the present work with a consequently lower absolute overpressure. Cubbison *et al.*² measured via pressure orifices in the flat plate just ahead of the injection pressure coefficients up to 0.70 for the jet interaction flow field with a freestream Mach number of 3.0 and a PR of 677. Also, the pressure distribution measured in the same experiment resembles very closely that predicted by the present numerical simulation,

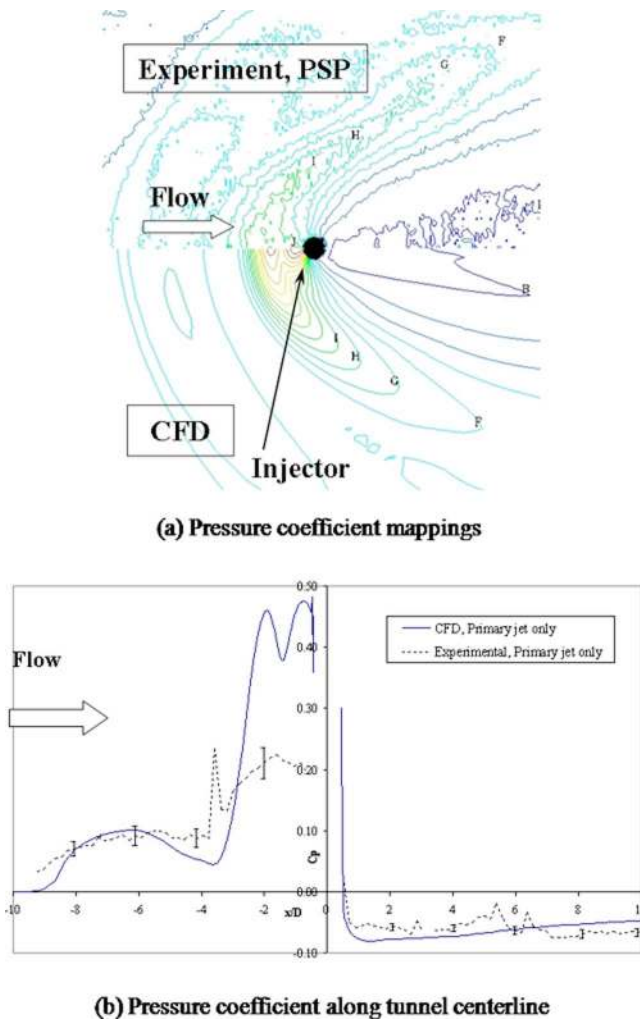


FIG. 11. (Color online) Comparison of the experimental and CFD pressure coefficient. (a) Mappings on surface of flat plate and (b) along the tunnel center line. The experimental data were obtained through PSP. $Ma=4.0$, $PR=532$ [Viti *et al.* (Ref. 26)].

with a high plateau corresponding to the separation region followed by a sharp peak created by the bow shock. Part of the discrepancy is attributable to the weaknesses associated with an eddy-viscosity model in which the assumption of isotropic turbulence might not hold true for the region with very high-pressure gradients and highly rotating flows. Unfortunately the lack of more accurate experimental data for the present case prevents a more complete validation of the numerical procedure. While these comparisons do not quantitatively validate the numerical solution, they provide a level of confidence necessary to proceed with the qualitative analysis of the flow field.

C. Vortical structures of the supersonic jet interaction flow field

A valuable insight of the jet interaction flow field and its vortical structures is provided by the isometric view of the flow near the injector, as shown in Fig. 12. This snapshot shows the Mach number contours mapped on the plane of symmetry [compare with Fig. 5(a)], the C_p contours on the surface of the flat plate and the vorticity magnitude contours

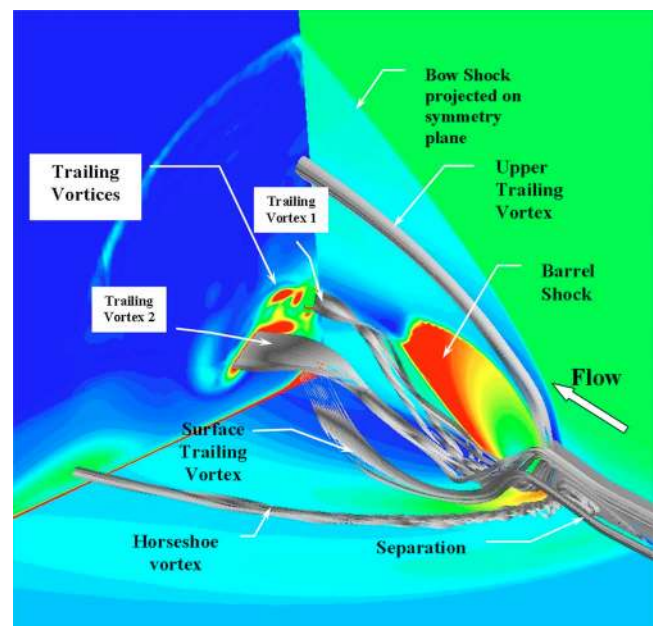


FIG. 12. (Color online) Isometric view of the flow around the injector with streamlines highlighting the main vortical structures. Mach number contours on symmetry plane, C_p contours on surface of flat plate, vorticity magnitude contours on cross plane.

on the cross plane aft of the barrel shock. The paths of the trailing vortices are highlighted by streamlines that follow the vortex core. The interpretation of the flow features of Fig. 12 is enhanced by the use of the two-dimensional pressure plots of Fig. 7. Following the flow along its path as indicated by the arrow, the first flow conditions to be encountered are those produced by the undisturbed freestream, region 1 of Fig. 7(a). The inlet boundary layer is clearly visible at the extreme left of Fig. 5(a) where the Mach number on the surface of the flat plate is zero, and it gradually increases until it reaches the freestream conditions. The turbulent boundary layer is allowed to grow freely along the flat plate surface to the location of the separation. Separation [see Fig. 10 and region 2 of Figs. 7(a) and 7(b)] is caused by the shock-boundary layer interaction. The strong adverse pressure gradient caused by the bow shock propagates upstream through the subsonic region of the boundary layer. In Fig. 7(a), the C_p plot along the center line shows the onset of separation as a region where the pressure increases steeply (region 2), then it plateaus and decreases again (region 3). The C_p contours of Fig. 7(b) show the separation as a well-defined lobe near the plane of symmetry [corresponding to regions 2 and 3 of Fig. 7(a)] that extends downstream and away from the tunnel center line. Region 3 is also where the core of the horseshoe vortex forms and is shed sideways from the symmetry plane as highlighted by the streamlines of Fig. 12. On the plane of symmetry the core of the horseshoe vortex appears as the upstream vortex of a pair of counter-rotating vortices, see Fig. 13. The progression of the horseshoe vortex as it trails downstream is also evident in the cross sectional mappings of the vorticity shown in Fig. 14. In these mappings the vortex is shown as a localized region of high-vorticity intensity close to the bottom surface and mov-

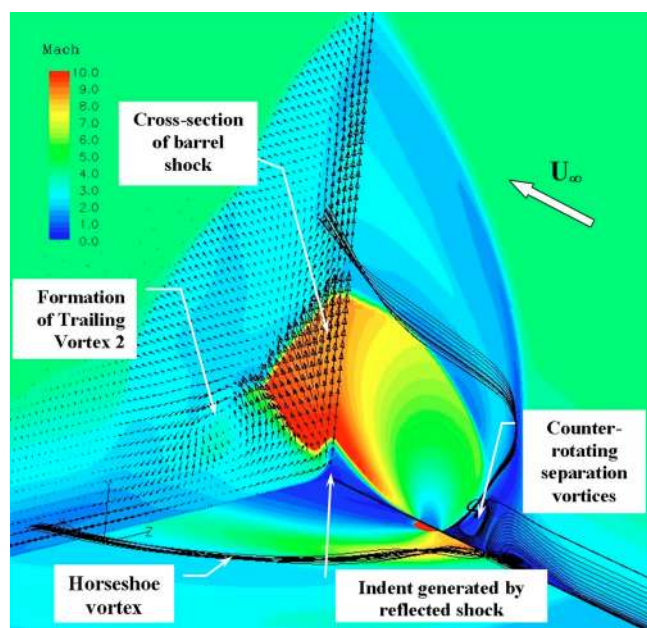


FIG. 13. (Color online) Detail of the isometric view of the oblique barrel shock with two groups of streamlines highlighting the flow in the recirculation region. Mach numbers contours are plotted on the cross plane and plane of symmetry, C_p contours on the flat plate surface. Velocity vectors (y - z projection) superimposed on the cross plane.

ing away from the plane of symmetry with downstream distance. The Mach number contours of Fig. 5(a) show the presence of a separation-induced shock. This oblique shock is not as strong as the bow or barrel shock as it is generated by the sudden thickening of the separated boundary layer, and it impinges on the upstream side of the bow shock. The boundary between regions 3 and 4, where the pressure along the center line decreases ($x/d = -4.0$), defines the stagnation location between the two counter-rotating vortices both of which are clearly visible through the streamlines of Fig. 13. They rotate in opposite directions and, on the center plane, their vorticity is normal to the incoming cross flow. However, as both vortices move away from the center line, their vorticity is realigned in the streamwise direction by the cross flow. The two vortices are divided by an attachment line [region 5 in Fig. 7(a)], indicated as a peak in the C_p plot. The rotation of the second (downstream) vortex is dictated by the direction of the injectant flow as it exhausts from the upstream rim of the orifice. Note the symmetry in the trends of the C_p distribution about region 5 in Fig. 7(a). Upstream (region 4) and downstream (region 6) of region 5 the pressure drops rapidly, and then it recovers to some level in regions 3 and 7. The pressure drop corresponds to the acceleration of the fluid moving away from the attachment line and the formation of the core of the two counter-rotating vortices. The pressure rise corresponds to the fluid moving away from the attachment line while being slowed down and turned around either by the incoming boundary layer fluid, as in the case for the upstream vortex in region 5, or by the barrel shock as for the downstream vortex, aft of region 5. The pressure peaks in regions 6 and 7 of Fig. 7(a) are also visible in the pressure mapping of Fig. 7(b) as the two small

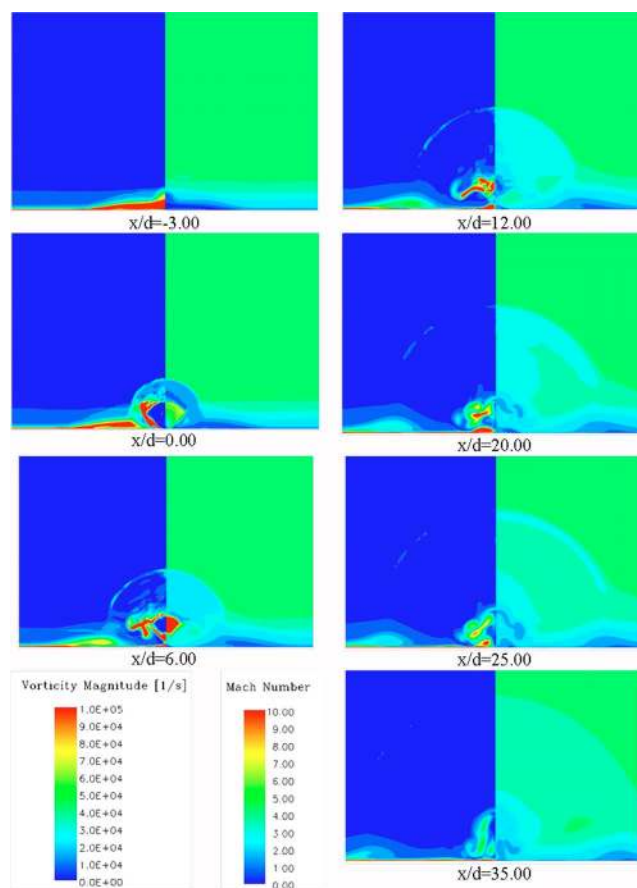


FIG. 14. (Color online) Cross plane mappings of vorticity magnitude (left) and Mach number (right).

lobes with the highest C_p values just in front of the injector. The two high-pressure lobes merge together as they move away from the centerline and trail downstream to form the footprint of the bow shock on the flat plate. In their numerical analysis of the two-dimensional jet interaction flow field, Chenault and Beran⁴⁹ reported a tertiary vortex in the separation region, rotating counterclockwise and located between the core of the horseshoe vortex and the flat plate. In the present study, no tertiary vortex was present in the separation region. This discrepancy could be due to the fact that the tertiary vortex is a feature of the two-dimensional jet interaction flow field only. In fact, the same authors did not report the existence of this vortex for the 3D numerical simulation of the jet interaction flow field.⁵⁰

As discussed above, the first of the two counter-rotating vortices in the separation region create one strong vortical structure that is the horseshoe vortex. The second counter-rotating vortex does not generate one single coherent structure but rather it generates several smaller vortical structures that trail downstream and around the barrel shock. One of these trailing vortices stemming from the separation region is the upper trailing vortex. This vortex is formed by the recirculating fluid close to the plane of symmetry, and it follows the leading edge of the barrel shock away from the solid surface. The core of this vortex is clearly visible in Fig. 12 and with more detail in the close-up of Fig. 13. As this vor-

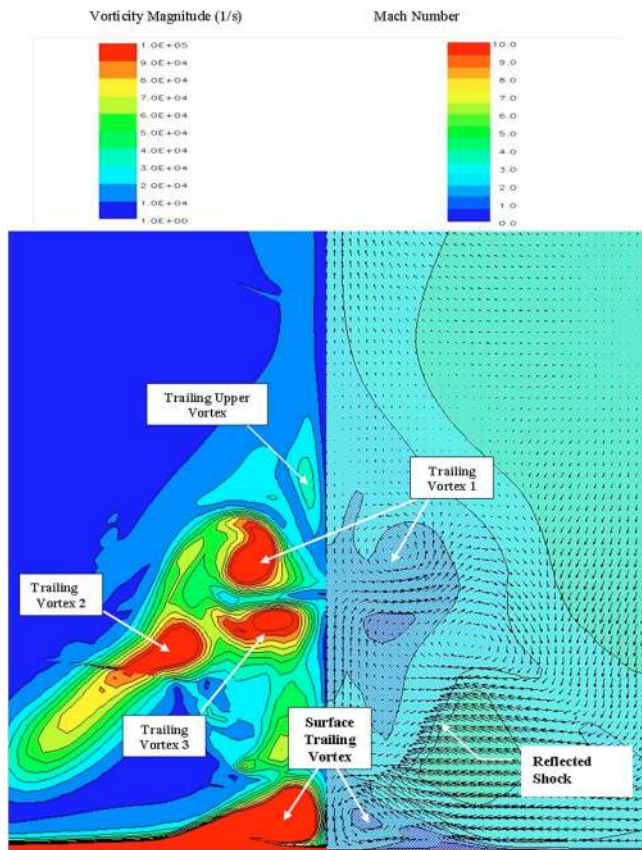


FIG. 15. (Color online) Cross plane mappings of vorticity magnitude (left) and Mach number (right) with velocity vectors superimposed at a location of $x/d=15.00$ downstream of the injector. The flow is into the plane of the page.

tex trails downstream, it moves away from the solid surface and away from the plane of symmetry, as shown in Fig. 14.

The rest of the fluid in the second counter-rotating vortex is convected downstream sideways, close to the surface of the flat plate and around the footprint of the barrel shock to form the surface trailing vortex. As shown by Fig. 12, the fluid that forms the core of the surface trailing vortex moves away from the symmetry plane as the barrel shock expands around the injector. When the barrel shock detaches from the surface of the flat plate, the surface trailing vortex moves toward the center line and into the low-pressure region behind the injector. Due to its proximity to the solid surface, the trailing vortex entrains large quantities of low-momentum boundary layer fluid, as is evident from Fig. 15. This presence of the trailing vortex and its behavior are in agreement with the observations of Palekar *et al.*⁵¹ However these authors did not report finding any vortical formation that resembles the upper trailing vortex and presently it is not clear why there exists this discrepancy between the two sets of results.

While the present work did not focus on the mixing of the injectant with the freestream, we can infer that such mixing is enhanced by the action of four distinct pairs of counter-rotating trailing vortices. The cores of the four vortices are highlighted in Fig. 15 through the plot of the vorticity magnitude on a cross flow plane at 15 jet diameters

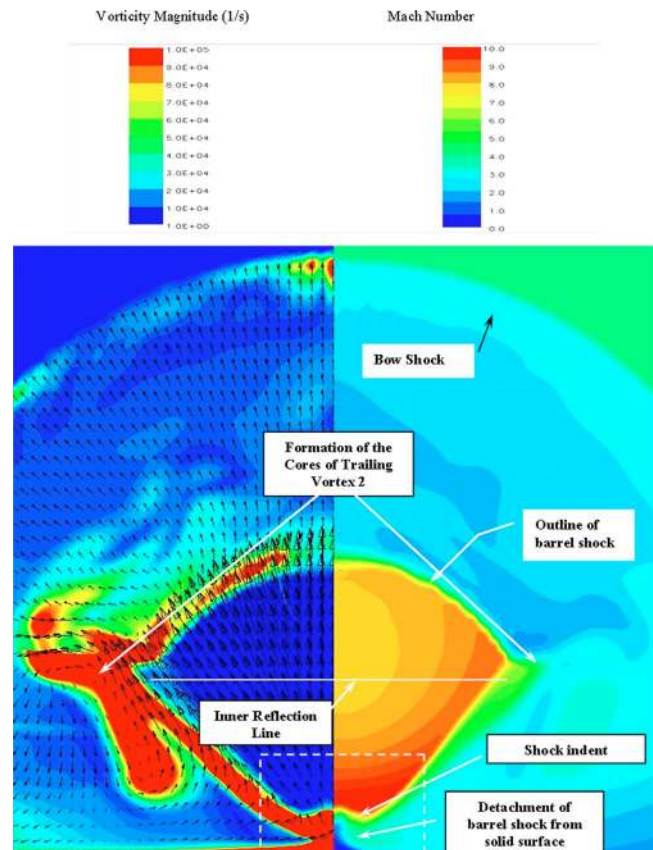


FIG. 16. (Color online) Cross plane mappings of vorticity magnitude (left) with projected velocity vectors and Mach number (right) with velocity vectors superimposed at a location of $x/d=3.5$ downstream of the injector. The flow is into the plane of the page. The dashed box represents the flow region that is magnified in Fig. 18(a).

downstream of the injection location. The surface trailing vortex was discussed earlier, and it was shown that it originates from the second counter-rotating vortex of the separation region and is energized by the shear layer of the barrel shock. Almost all of the fluid contained in the core of this vortex is freestream fluid. The trailing vortex 1 and trailing vortex 3 are a couple of counter-rotating vortices formed as the slow-moving injectant fluid comes in contact with the high-speed cross flow aft of the Mach disk, as shown in Figs. 12 and 14 for x/d of 6.00 and 12.00. Most of the fluid contained in these two vortices is injectant fluid, with small quantities of freestream fluid being entrained from the shear layer between the barrel shock and the freestream. Relatively little mixing with the freestream occurs until a location 30 diameters downstream of the injection location. The fourth vortex shown in Fig. 15 is trailing vortex 2. This vortex forms in the shear layer region existing between the windward side of the injector and the second of the two counter-rotating vortices. Part of the vortex fluid is injectant fluid entrained from the windward side of the barrel shock. The vortex core forms on the center line, and it is convected downstream and upward along the sharp angle in the barrel shock, as shown in Fig. 16. Figure 16 also shows the mechanism that moves the surface trailing vortices toward the center line. As the barrel shock detaches from the solid surface

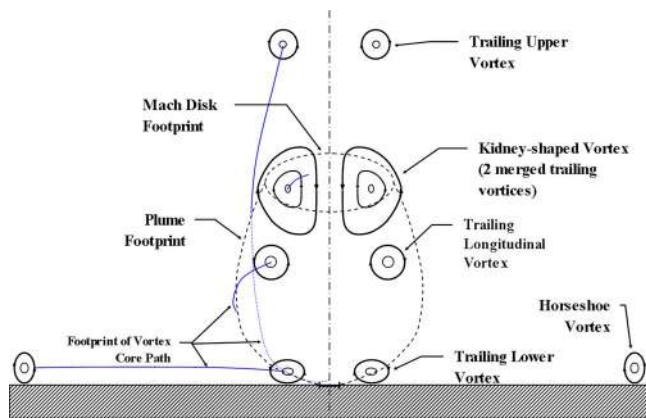


FIG. 17. (Color online) Schematic of the flow field at a transverse section aft of the barrel shock.

of the flat plate, it creates the low-pressure region which is occupied by the vortex. Initially, trailing vortex 2 is bounded by the plate surface and the bottom side of the barrel shock. As shown in Fig. 14, the three upper vortices (trailing vortices 1, 2, and 3) rotate with respect to each other around a common longitudinal axis (see Figs. 14 and 15, $x/d=20.0$). As they trail downstream, they merge into a single vortex (see Fig. 14, $x/d=35.0$) that is the main mechanism driving the mixing of the freestream fluid with the injectant. The horseshoe vortex and the trailing upper vortices continue to be convected downstream along their trajectories and do not contribute to the mixing of the injectant with the freestream; see, for example, Figs. 7 and 14 at locations $x/d=35.0$ and 40.0.

A summary of the vortical structures found in the present study of the supersonic jet interaction flow field is shown in Fig. 17. This figure shows a schematic of the cross flow section at a location aft of the barrel shock. A system of five pairs of counter-rotating vortices forms in the recirculation region ahead of the injector, along the barrel shock wave and immediately downstream of the Mach disk. Of these ten vortices, eight form in the recirculation region, and the other pair is formed by the recompression of the jet fluid passing through the Mach disk. This vortex is generally referred to as the kidney-shaped vortex, see Ref. 52 for details. The horseshoe vortex and the trailing upper vortex systems form and immediately move away from the centerline of the plate. The horseshoe vortex moves horizontally along the solid surface and away from the symmetry plane while the upper vortex moves vertically along the symmetry plane and away from the flat plate surface (see Fig. 17). The longitudinal vortices form in the recirculation region and gain in strength as they are convected downstream and upwards along the barrel shock plume. The trailing lower vortices also form in the recirculation region, but they remain close to the surface and to the plane of symmetry. The kidney-shaped counter-rotating vortices form downstream of the jet plume and are the major contributors to the mixing of the injectant with the freestream, mainly by entrainment of the freestream in the vortices. Both the horseshoe and the upper vortex systems trail downstream isolated from the other vortex systems. The upper vortex is weaker than the other systems hence more

difficult to identify and to follow in the cross sectional mappings. It appears clearly defined in the vorticity mappings of Fig. 15 and as the streamlines of Fig. 12. The lower trailing vortex remains attached to the solid surface as it entrains fluid from the surrounding boundary layer. The other two vortex systems, the longitudinal, and kidney-shaped vortex systems, merge aft of the Mach disk into a single vortex that trails downstream along a constant cross plane location. This system of three trailing vortices was also reported in the numerical study of Tam and Gruber.²⁴

It is of interest to notice the major differences between the vortical formations observed in the subsonic and in the supersonic jet interaction flow field. In the subsonic jet interaction flow field the main mechanism responsible for the formation of the longitudinal trailing vortices is the realignment of the vorticity present in the injector boundary layer. These vortices are shed intermittently and form a double-deck structure with the pair of stable vortices stacked above them.⁹ In the supersonic flow field, the majority of the vortical structures are formed by the shock waves and the separation region ahead of the injector. Although in the present study a boundary layer was not simulated inside the injector, the high expansion of the injectant fluid suggests that the flow field inside the barrel shock is dominated by inviscid rather than viscous phenomena. The assumption of a step profile for the injector, corrected for viscous effects through the discharge coefficient, is a common practice in the numerical study of choked nozzles exhausting either in a quiescent medium or in a cross flow.^{24,28–31,49,50} Further, in the supersonic flow field the largest contribution to the generation of vorticity is primarily due to the entropy changes generated by the shocks rather than the direct interaction of the injectant with the cross flow boundary layer.

D. Features of the barrel shock

Two prominent features differentiate the barrel shock formed by an underexpanded sonic jet exhausting in a quiescent medium from the case with a cross flow. These two features are (a) the barrel shock indentation created by the reflection of the shock itself on the flat plate, and (b) the inner shock reflection line caused by the folding of the windward side of the barrel shock into itself. The barrel shock indent was introduced previously in the analysis of Figs. 13 and 16. The latter clearly shows the sharp angle formed by the reflected shock penetrating into the main shock. The shock reflection is caused by the downstream tilt of the barrel shock axis. Due to the tilt, the injectant on the downstream side of the barrel shock does not have space to expand and recompress through the barrel shock to the correct local pressure. For this reason, the barrel shock is attached to the surface of the flat plate just downstream of the injector, as shown in the side view of Fig. 5(b) and in the cross section of Fig. 14 ($x/d_j=0.0$). The presence of the solid surface creates a reflection of the barrel shock that moves back inward into the barrel shock. Due to the curvature of the barrel shock, the shock boundary tangential to the surface of the flat plate is reflected first, thus creating the concave triangular indent observed in Figs. 14 and 16 at $x/d_j=6.0$. A closer

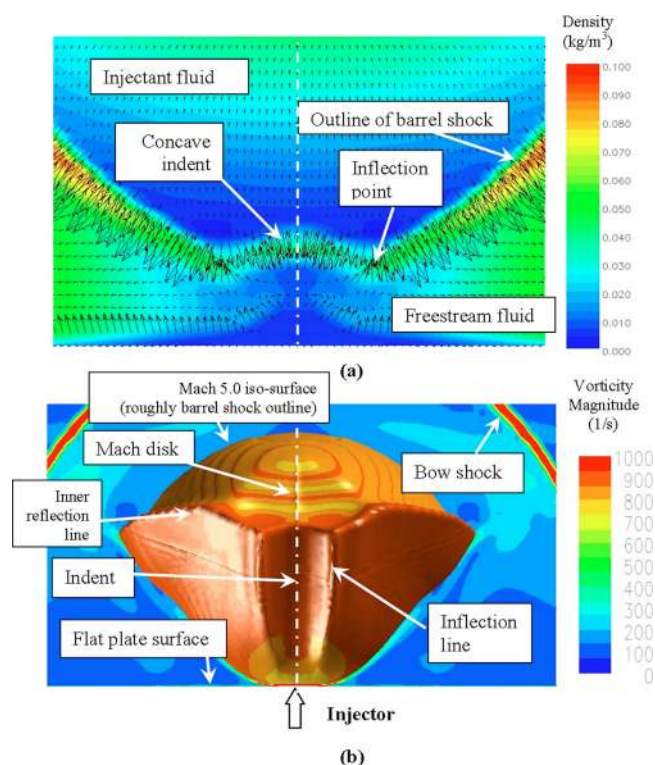


FIG. 18. (Color online) Downstream view of the indent in the barrel shock created by the reflection of the compression wave on the surface of the flat plate downstream of the injection location. The flow is out of the plane of the page. (a) Detailed view of the indent. Density gradient contours on a cross plane at $x/d_j = 3.5$. (b) Downstream view of the barrel shock represented by the MACH 5.0 isosurface. Cross plane is colored by vorticity magnitude.

view of the indent is shown in Fig. 18(a), which represents a detail of the dashed box of Fig. 16. The vectors represent the density gradient, and the contours represent the magnitude of the density gradient. The right side of the mapping shows the curved cross section of the barrel shock, with injectant fluid on its inside (top half of picture) and freestream fluid on the outside (lower half of picture). The concave indentation is located in the proximity of the plane of symmetry since it is at this location only that the barrel shock is in contact with the flat plate. The shape of the indent resembles in thickness and curvature an inverted continuation of the barrel shock. The movement of the recompression shock away from the solid surface creates the region of low pressure in the proximity of the center line. The footprint of this low-pressure region on the flat plate, as shown in Fig. 7(b), is a result of the indent in the barrel shock. The low-pressure lobes [contours B and C in Fig. 7(b)] that appear to extend along a radial line from the injector correspond to the inflection lines of the barrel shock cross section shown in Fig. 18(a). The effect of the indentation on the general shape of the barrel shock is clearly shown by the isosurface of Fig. 18(b), where the surface corresponding to a Mach number of 5.0 is highlighted. The background mapping is colored with the magnitude of vorticity on a cross plane at $x/d_j = 1.0$. The isosurface highlights the three dimensionality of the indent that forms a channel in the leeward side of the barrel shock. The presence of the concave channel creates a local region of low pressure

that makes the surface trailing vortex move closer to the center line. Again, the footprint of the low-pressure region in Fig. 7(b) is correlated with the indent channel and inflection lines. Also the indent channel clips the lower side of the Mach disk. The relationship between the concave channel in the barrel shock created by the reflection of the shock from the solid surface and the low-pressure in the region aft of the jet is relevant to jet-thruster control system applications. According to the present analysis, the low-pressure region could be minimized by allowing the injectant to equalize its pressure to the local freestream pressure without the interference of the solid surface. This could be achieved by designing the surface of the flat plate immediately aft of the jet as a concave surface that would accommodate without interference the volume of the barrel shock. This design philosophy is opposite to that pursued by Byun *et al.*¹⁹ and Viti *et al.*⁸ who attempted to decrease the low-pressure region by using a protrusion in the solid surface, either in the form of a 3D solid ramp or an array of secondary jets to create and aerodynamic ramp. The design with a concave surface would have the advantage of being low-drag and simple to implement with no actuating or moving parts.

Figure 18(b) shows the second feature that distinguishes the barrel shock formed by an underexpanded jet in a quiescent environment from that with a cross flow, i.e., the internal reflection line. The internal reflection line is created by the folding of the windward side of the barrel shock onto itself due to the localized high backpressure that exists due to the presence of the bow shock on this side of the injector. The expansion fan in Fig. 5(b) shows that the injectant expands symmetrically in the region near the nozzle. However, on the upstream side of the nozzle, the high pressure generated by the compression of the freestream fluid passing through the bow shock, causes the expanding injectant to recompress earlier than on the downstream side of the nozzle. The recompression shock on the windward side of the barrel shock is pushed downstream by the incoming freestream flow, thus breaking the symmetry of the expanding jet. Notice in Fig. 5(b) how the injectant can expand to much lower pressure and higher Mach numbers on the leeward side of the barrel shock where the local backpressure is lower than the windward side. The deformation of the barrel shock due to the internal reflection line is clearly shown by the MACH 5.0 isosurface of Fig. 19, which is a side cross section along the plane of symmetry of Fig. 18(b). The background contours represent the Mach number on a longitudinal plane at $z/d_j = 5.0$. The use of the Mach number isosurface allows the analysis of the 3D features found in the interior of the barrel shock. Inside the barrel shock, the first MACH 5.0 surface is visible enveloping the injector. This surface appears to be symmetrical about the injector, and it is formed by the expansion of the sonic jet. The second isosurface represents the approximate boundary of the barrel shock as it denotes the location at which the injectant is recompressed to the local static pressure. The internal reflection line is clearly visible as a straight line that starts upstream at the location where the expanding injectant loses its symmetry and ends at the downstream side of the barrel shock. Notice also the presence of the indent line that does not

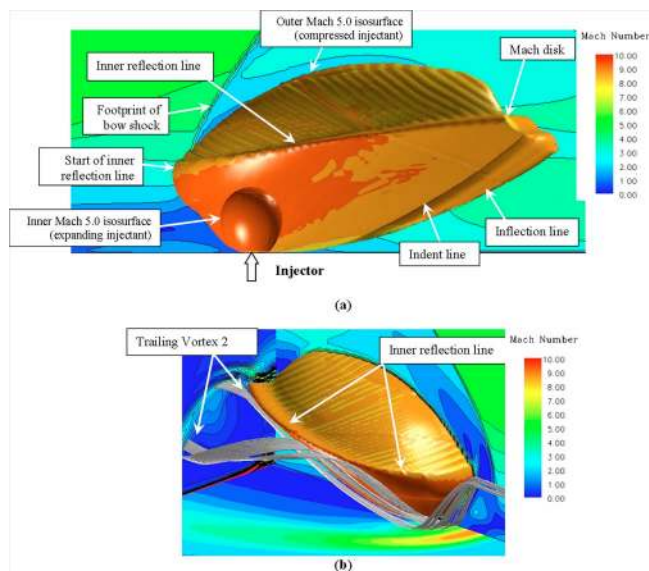


FIG. 19. (Color online) (a) Side view of the inside of the barrel shock represented by MACH 5.0 isosurfaces also shown in Fig. 18(b). The colored contours represent Mach number on a plane at $z/d_j=5.0$ from the plane of symmetry. (b) Isometric view of the MACH 5.0 isosurface. The contours on the plane of symmetry represent Mach number, on the flat plate pressure coefficient and on the cross plane vorticity magnitude.

appear in the contour plots on the plane of symmetry of Fig. 5 due to these plots being purely two dimensional. The incline angle of the inner reflection line is a function of the momentum flux ratio and of the local backpressure created by the freestream and the bow shock. The presence of the inner reflection line influences the flow field outside and around the barrel shock since a strong shear layer is generated by the injectant fluid expanding around the reflection line. When visualized through a Mach isosurface, the inner reflection lines appear as finlike structures that extend along the length of the barrel shock, as shown in Fig. 19(b). Notice that the inner reflection line is visible in the Schlieren picture of Fig. 9 on the windward side of the barrel shock.

E. Oil surface-flow results

Relevant information on the mechanisms that create the pressure field on the flat plate can be obtained by the oil surface-flow visualization shown in Fig. 20. In this figure, streamlines are drawn just above the surface so as to highlight the projection of the two-dimensional velocity field above the surface. It is important to bear in mind that this is a two-dimensional representation of a 3D flow and therefore, there are velocity components that are moving into (or out of) the plane of these streamlines. The major flow structures such as the bow shock, the separation and the barrel shock are clearly visible as thicker oil lines. The freestream appears undisturbed until the bow shock. Behind the bow shock the freestream assumes a lateral velocity component to compensate for the volume occupied by the barrel shock. In the separation region, the fluid is turned around by the two counter-rotating vortices and flows in the opposite direction as the freestream. The local pressure is higher than the freestream. As discussed before, the pair of horseshoe vortices

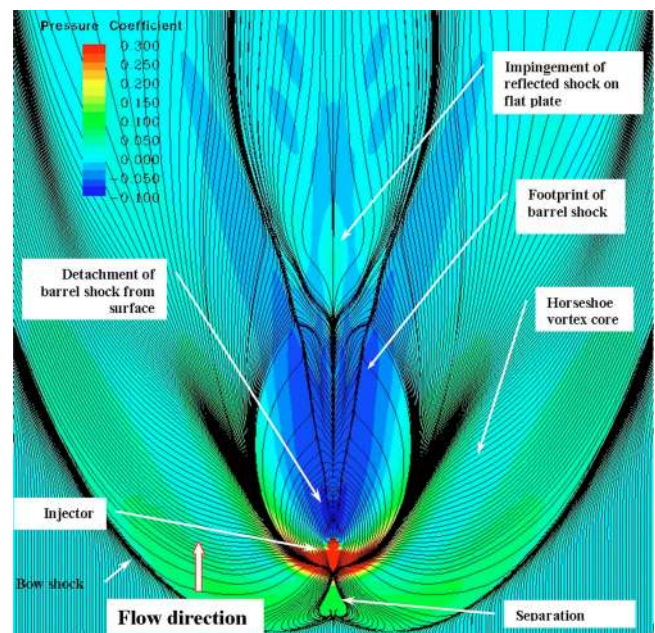


FIG. 20. (Color online) Streamlines above the flat plate simulating oil surface-flow visualization with pressure coefficient mapping superimposed.

is shed from the most upstream of the two counter-rotating vortices in the separation region. The core of the horseshoe vortices can be traced by following the low-pressure lobe on the solid surface [see also the mapping of Fig. 7(b)]. Immediately aft of the injector, there is a small region where the plume is attached to the solid surface. The oil-flow shows the footprint of the concave indentation in the leeside of the barrel shock, analyzed in Sec. III D. The footprint of the barrel shock is clearly visible on the surface as are the attachment lines of the surface trailing vortices. At the location at which the plume becomes detached from the solid surface, a low-pressure region forms, and the surface trailing vortices are pulled together toward the plane of symmetry. Further downstream, the reflected shock from the Mach disk impinges on the solid surface. The local increase in pressure along the centerline [see the C_p plot of Fig. 7(a), regions 10 and 11] causes the surface trailing vortices to move away from the symmetry plane. Once past this location, the surface trailing vortices return to move parallel to the symmetry plane and the pressure recovers to the freestream value. This flow pattern is similar to that observed by Palekar *et al.*⁵¹ through the use of 3D streamlines. In their analysis, the impingement of the shock on the flat plate is clearly indicated by a lateral movement in the path of the streamlines, a similar behavior to that observed in Fig. 20.

IV. CONCLUSIONS

Numerical simulations of the 3D jet interaction flow field produced by a sonic circular jet exhausting normally into a turbulent supersonic cross flow over a flat plate were performed to study the time-averaged flow features that characterize this fluid-dynamic problem. The numerical computations made possible a detailed analysis of the prominent features that dominate the flow field. Through comparison

with experimental data, the solution was found to capture the typical shock formations such as the bow shock, the barrel shock wave, and the separation-induced shock wave. These compressible flow features were found to be closely coupled with a complex system of vortical structures that dominate the flow field. In particular, the trailing vortices were found to be generated by the cross flow that, after being compressed by the bow shock, has to move around the barrel shock and mix with the expanding injectant fluid. The pressure distribution on the flat plate was correlated with the aforementioned flow features. The nose-down pitching moment typical of the jet interaction flow field was found to result from the coupling of the high pressure in the separation region ahead of the injector with the low-pressure region aft of the injector. The high-pressure region corresponding to the separation exhibits localized pressure maxima and minima. These local peaks in pressure are generated by the presence of two counter-rotating vortices that impinge on the surface of the flat plate, the pressure peaks corresponding to local stagnation conditions and the pressure troughs to the vortical flow moving away from the surface. The low-pressure region aft of the injector was found to be created primarily by the reflection of the barrel shock on the solid surface of the flat plate. This reflection creates a concave indent in the leeward side of the barrel shock that promotes the lowering of the local pressure. The footprint of the low-pressure region on the flat plate with its two prominent lobes extending far downstream was correlated with the 3D concave channel that the shock reflection creates in the back side of the barrel shock. The lack of symmetry in the backpressure, the windward pressure being higher than the leeward side also creates an inner reflection plane in the barrel shock. In particular, the inner reflection was found to be generated by the folding of the windward side of the barrel shock into itself, thus creating a truncated and leaning barrel shock formation. The inner reflection line was observed to appear as a finlike structure on the lateral sides of the barrel shock and it promotes the formation of one major vortical structure, trailing vortex 2 and the mixing of the injectant with the freestream fluid.

ACKNOWLEDGMENTS

The authors would like to thank Dr. William McGrory for his invaluable advice and for granting the authors access to the computational resources and software of AeroSoft, Inc. Funding for the present study was granted by the Air Force Research Laboratory under Contract No. AFR-2T-3014-AOS.

¹AGARD, "Computational and experimental assessment of jets in cross-flow," AGARD Conference Proceedings No. 534, Winchester, United Kingdom, April 1993.

²R. B. Cubbison, B. H. Anderson, and J. J. Ward, "Surface pressure distributions with a sonic jet normal to adjacent flat surfaces at Mach 2.92 to 6.4," NASA Technical Note No. TN D-580, 1961.

³J. Brandeis and J. Gill, "Experimental investigation of super- and hypersonic jet interaction on missile configurations," *J. Spacecr. Rockets* **35**, 296 (1998).

⁴F. W. Spaid, E. E. Zukoski, and R. Rosen, "A study of secondary injection of gases into a supersonic flow," NACA Technical Report No. 32-834, Jet

Propulsion Laboratory, California Institute of Technology, Pasadena, CA, August 1966.

⁵V. Viti, J. A. Schetz, and R. Neel, "Numerical studies of the jet interaction flowfield with a main jet and an array of smaller jets," International Congress of Aeronautical Sciences, Toronto, Canada, September 2002, ICAS Paper 2002-4.7.1.

⁶V. Viti, "Numerical studies of the jet interaction flowfield with a main jet and an array of smaller jets," Ph.D. dissertation, Virginia Tech, September 2002.

⁷R. Chamberlain, D. McClure, and A. Dang, "CFD analysis of lateral jet interaction phenomena for the THAAD interceptor," 38th AIAA Aerospace Sciences Meeting, 10–13 January 2000, AIAA Paper No. 00-0963.

⁸V. Viti, S. Wallis, J. A. Schetz, and R. Neel, "Jet interaction with a main jet and an array of smaller jets," *AIAA J.* **42**, 1358 (2004).

⁹B. A. Haven and M. Kurosaka, "Kidney and anti-kidney vortices in cross-flow jets," *J. Fluid Mech.* **352**, 27 (1997).

¹⁰R. C. Orth, J. A. Schetz, and F. S. Billig, "The interaction and penetration of gaseous jets in supersonic flow," NASA Contractor Report No. CR-1386, July 1969.

¹¹W. Letko, "Loads induced on a flat plate at a Mach number of 4.5 with a sonic or supersonic jet exhausting normal to the surface," NASA Technical Note No. D-1935, 1963.

¹²P. F. Hawkins, H. Lehman, and J. A. Schetz, "Structure of highly under-expanded transverse jets in a supersonic stream," *AIAA J.* **5**, 882 (1967).

¹³F. S. Billig and J. A. Schetz, "Penetration of a fluid jet into a supersonic stream," *J. Spacecr. Rockets* **3**, 1658 (1966).

¹⁴J. A. Schetz, *Injection and Mixing in Turbulent Flow*, Progress in Astronautics and Aeronautics, Vol. 68 (AIAA, Reston, VA, 1980).

¹⁵F. W. Spaid and E. E. Zukoski, "Secondary injection of gases into a supersonic flow," *AIAA J.* **2**, 1689 (1964).

¹⁶A. I. Glagolev, A. I. Zubkov, and Y. A. Panov, "Supersonic flow past a gas jet obstacle emerging from a plate," *Fluid Mech.-Sov. Res.* **2**, 97 (1979).

¹⁷A. I. Glagolev, A. I. Zubkov, and Y. A. Panov, "Interaction between a supersonic flow and gas issuing from a hole in a plate," *Fluid Mech.-Sov. Res.* **3**, 99 (1979).

¹⁸D. M. Voitenko, A. I. Zubkov, and Y. A. Panov, "Existence of supersonic zones in three-dimensional separation flows," *Fluid Mech.-Sov. Res.* **2**, 20 (1979).

¹⁹Y. H. Byun, K. J. Bae, S. Wallis, V. Viti, J. A. Schetz, and R. Bowersox, "Jet interaction in supersonic flow with a downstream surface ramp," *J. Spacecr. Rockets* **42**, 38 (2005).

²⁰J. A. Schetz, S. Cox-Stouffer, and R. Fuller, "Integrated CFD and experimental studies of complex injectors in supersonic flows," AIAA Paper No. 98-2780, June 1998.

²¹L. Maddalena, T. L. Campioli, J. A. Schetz, "Experimental and computational investigation of an aeroramp injector in a Mach four cross flow," 13th International Space Planes and Hypersonics Systems and Technologies, Capua, Italy, 16–20 May 2005, AIAA Paper No. 2005-3235.

²²D. C. Wilcox, "Comparison of two-equation turbulence models for boundary layers with pressure gradient," *AIAA J.* **31**, 1414 (1993).

²³D. C. Wilcox, *Turbulence Modeling for CFD*, 2nd ed. (DCW Industries, La Canada, CA, 1998).

²⁴C.-J. Tam and M. R. Gruber, "Numerical study of jet injection into a supersonic crossflow," 35th AIAA Joint Propulsion Conference, Los Angeles, CA, 20–24 June 1999, AIAA Paper No. 99-2254.

²⁵J. L. Payne, C. J. Roy, and S. J. Beresh, "A comparison of turbulence models for a supersonic jet in transonic cross flow," 39th AIAA Aerospace Science Meeting and Exhibit, January 2001, AIAA Paper No. 2001-1048.

²⁶V. Viti, J. A. Schetz, and R. Neel, "Comparison of first and second order turbulence models for a jet/3D ramp combination in supersonic flow," 43rd AIAA Aerospace Sciences Meeting and Exhibit, January 2005, AIAA Paper No. 2005-0499.

²⁷F. R. Menter, "Zonal two equation $k-\omega$ turbulence models for aerodynamic flows," AIAA Paper No. 93-2906, July 1993.

²⁸R. P. Roger and S. C. Chan, "Parameters affecting penetration of a single jet into a supersonic crossflow: A CFD study—II," AIAA Paper No. 98-0425, January 1998.

²⁹A. Nedungadi and M. J. Lewis, "A numerical study of fuel mixing enhancement using oblique shock/vortex interactions," AIAA Paper No. 96-2920, February 1997.

³⁰A. Nedungadi and M. J. Lewis, "Computational study of three-dimensional shock-vortex interaction," *J. Aircr.* **34**, 2545 (1996).

³¹T. Hsieh, "Analysis of the scaling effects for missile configuration with lateral thruster," AIAA Paper No. 99-0810, January 1999.

- ³²J. McDaniel, C. Glass, D. Staack, and C. Miller, "Experimental and computational comparison of an under-expanded jet flowfield," AIAA Paper No. 2002-0305, January 2002.
- ³³AeroSoft, Inc., GASP 3.2 User Manual, 1997.
- ³⁴AeroSoft, Inc., GASP 4.0 User Manual, 2001.
- ³⁵J. C. Tannehill, D. A. Anderson, and R. H. Pletcher, *Computational Fluid Mechanics and Heat Transfer*, 2nd ed. (Taylor & Francis, London, 1997).
- ³⁶K. M. Peery and S. T. Imlay, "Blunt-body flow simulations," AIAA Paper No. 88-2904, 1988.
- ³⁷Pointwise, Inc., GRIDGEN version 13.3 User Manual, 1999.
- ³⁸M. Vinokur, "On one-dimensional Stretching functions for finite difference calculations," *J. Comput. Phys.* **50**, 215 (1983).
- ³⁹J. E. Bardina, P. G. Huang, and T. J. Coakley, "Turbulence modeling validation, testing and development," NASA Technical Memorandum No. TM 110446, April 1997.
- ⁴⁰P. J. Roache, *Verification and Validation in Computational Science and Engineering* (Hermosa, Albuquerque, NM, 1998).
- ⁴¹C. J. Roy, "Grid convergence error analysis for mixed-order numerical schemes," AIAA Paper No. 2001-2006, June 2001.
- ⁴²T. R. Fric and A. Roshko, "Vortical structure in the wake of a transverse jet," *J. Fluid Mech.* **279**, 1 (1994).
- ⁴³M. R. Gruber, A. S. Nejad, T. H. Chen, and J. C. Dutton, "Transverse injection from circular and elliptical nozzles into a supersonic crossflow," *J. Propul. Power* **16**, 449 (2000).
- ⁴⁴S. Murugappan, E. Gutmark, and C. Carter, "Control of penetration and mixing of an excited supersonic jet into a supersonic cross stream," *Phys. Fluids* **17**, 106101 (2005).
- ⁴⁵M. A. Woodmansee and J. C. Dutton, "Experimental measurements of pressure, temperature, and density in an under-expanded sonic jet flowfield," AIAA Paper No. 99-3600, June 1999.
- ⁴⁶M. A. Woodmansee, V. Iyer, J. C. Dutton, and R. P. Lucht, "Nonintrusive pressure and temperature measurements in an underexpanded sonic jet flowfield," *AIAA J.* **42**, 1170 (2004).
- ⁴⁷J. Olejniczak, M. J. Wright, and G. V. Candler, "Numerical study of inviscid shock interactions on double-wedge geometries," *J. Fluid Mech.* **352**, 1 (1997).
- ⁴⁸S. Wallis, "Innovative transverse jet interaction arrangements in supersonic crossflow," M.S. thesis, Virginia Tech, December 2001.
- ⁴⁹C. F. Chenault and P. S. Beran, " κ - ϵ and Reynolds stress turbulence model comparisons for two-dimensional injection flows," *AIAA J.* **36**, 1401 (1998).
- ⁵⁰C. F. Chenault, P. S. Beran, and R. D. Bowersox, "Numerical investigation of supersonic injection using a Reynolds-stress turbulence model," *AIAA J.* **37**, 1257 (1999).
- ⁵¹A. Palekar, C. R. Truman, and P. Vorobie, "Prediction of transverse injection of a sonic jet in supersonic cross flow," AIAA Paper No. 2005-5366, June 2005.
- ⁵²L. Cortelezzi and A. R. Karagozian, "On the formation of the counter-rotating vortex pair in transverse jets," *J. Fluid Mech.* **446**, 1347 (2001).